ADVANCED ENGINEERING MATERIALS
www.aem-journal.com

Mechanical and Microstructural Effects of ZrO_2 Nanoparticles in Fe20Cr Oxide Dispersion-Strengthened Alloys Processed by Laser Powder Bed Fusion

*Mareen Goßling, Silja-Katharina Rittinghaus, Felix Radtke, Abdelrahman Elsayed, Marina Macias Barrientos, Ulf Ziesing, Louis Becker, Ihsan Murat Kuşoğlu, Christoph Broeckmann, Ulrich Krupp, Avinash Hariharan, Sebastian Weber, and Bilal Gökce**

Integrating oxide nanoparticles (ONPs) into additively manufactured oxide dispersion-strengthened (ODS) steels is challenging due to their tendency for agglomeration and particle loss during processing. This study compares chemically synthesized and laser-generated ZrO_2 ONPs in Fe20Cr alloys produced by laser-based powder bed fusion (PBF-LB/M) using two concentrations (0.1 and 1.0 vol%) under comparable conditions. Oxide nanoparticle (ONP) properties, dispersion, and their impact on microstructure were analyzed via scanning electron microscopy, transmission electron microscopy, electron channeling contrast imaging, and X-ray fluorescence. Mechanical properties are evaluated through hardness, compression, and creep testing at 600 °C. Laser-generated ONPs exhibited narrower size distributions ($D_{90} = 10$ nm) and finer initial dispersion, enabling grain refinement and increased flow stress at 1.0 vol%, increased agglomeration lowered ONP dispersion and increased interparticle distance. Chemically synthesized ONPs show broader distributions and less uniform dispersion, but result in finer grains after heat treatment. Despite coarser grains, the sample with 1.0 vol% laser-generated ONPs shows the lowest creep rate, indicating that a sufficient ONP concentration with limited agglomeration is more critical for creep resistance than grain refinement alone. The results demonstrate that the ONP synthesis route and loading influence the microstructure and ONPs amount-specific strengthening, guiding the design of ODS steels for additive manufacturing.

1. Introduction

Oxide dispersion-strengthened (ODS) steels are known for their exceptional high-temperature strength and creep resistance, making them suitable for use in turbines, boilers, and fusion reactors under extreme thermal and mechanical loads.[1–3] Their performance results primarily from a uniform distribution of nanoscale oxide particles that impede dislocation motion via Orowan looping and grain boundary pinning.[4]

Conventional ODS production methods, such as mechanical alloying and hot isostatic pressing (HIP), are effective but energy-intensive, costly, and challenging to scale.[5–8] Additive manufacturing (AM), particularly laser-based powder bed fusion (PBF-LB/M), offers a promising alternative due to its geometric flexibility and processing efficiency.[9,10] However, integrating oxide nanoparticles (ONPs) into metallic matrices during AM remains challenging. Issues such as agglomeration,

M. Goßling, S.-K. Rittinghaus, B. Gökce
Chair of Materials Science and Additive Manufacturing
University of Wuppertal
42119 Wuppertal, Germany
E-mail: goekce@uni-wuppertal.de

F. Radtke, C. Broeckmann
Chair and Institute for Materials Applications in Mechanical Engineering
RWTH Aachen University
52062 Aachen, Germany

The ORCID identification number(s) for the author(s) of this article can be found under https://doi.org/10.1002/adem.202500317.

DOI: 10.1002/adem.202500317

A. Elsayed, U. Krupp, A. Hariharan
Chair of Materials Engineering of Metals at IEHK Steel Institute
RWTH Aachen University
52072 Aachen, Germany

M. M. Barrientos
Chair of Materials Test Engineering (WPT)
TU Dortmund University
44227 Dortmund, Germany

U. Ziesing, L. Becker, S. Weber
Chair of Materials Technology
Institute for Materials
Ruhr-Universität Bochum
44801 Bochum, Germany

I. M. Kuşoğlu
Technical Chemistry I
Center for Nanointegration Duisburg-Essen (CENIDE)
University of Duisburg
45141 Essen, Germany

inhomogeneous dispersion, and particle loss during melting can impair mechanical performance.[11–15]

Laser-based nanoparticle synthesis offers precise control over particle characteristics. Techniques like laser ablation in liquids (LALs) enable the production of high-purity nanoparticles with narrow size distributions and well-defined morphologies.[16–18] In the context of ODS steels, laser-synthesized ZrO_2 nanoparticles have shown particular promise.[19] Depending on process parameters, monoclinic, tetragonal, or cubic ZrO_2 phases can form, exhibiting different internal stress profiles and transformation behavior.[20,21] For example, tetragonal particles may exhibit residual stresses up to 6 GPa and undergo stress-induced transformations.[20] While production rates and productivity-related energy efficiencies vary, ranging from 0.3 to 25 $g\,h^{-1}$ and 8–83 $Wh\,h\,g^{-1}$, laser-based techniques offer a unique capability to tailor nanoparticle features like size and shape directly during synthesis.[22,23]

ZrO_2 is well-established for dispersoids in ODS steels, valued for its thermal stability and contribution to creep resistance.[24–28] Although chemically synthesized ZrO_2 has been widely used, the potential of laser-generated variants remains underexplored, particularly in alloys processed by AM. Smaller ONPs ($\leq$10 nm) have demonstrated strong strengthening effects,[29] yet their retention during AM is limited by their high reactivity.[30–32] Compared to more common dispersoids like Y_2O_3,[33–36] ZrO_2 also offers advantages in oxidation resistance and phase stability. However, the influence of the synthesis route on their behavior in AM remains insufficiently understood.

Benchmark values for ODS steels vary depending on the alloy composition and processing method. Conventionally processed 14Cr and 18Cr alloys can reach flow stresses of 300–460 MPa at elevated temperatures.[37–39] Widely used examples include PM2000 (Fe-20Cr-5Al), MA956, and 14YWT. However, these systems combine multiple strengthening effects. To isolate the role of the oxide, this study uses a binary Fe20Cr alloy, omitting elements such as Al or Ti, which typically contribute to complex secondary phase formation.[40–42]

Despite broad interest in ZrO_2 as a dispersoid, no quantitative study has yet compared the mechanical performance of AM-processed ODS steels as a function of ZrO_2 synthesis route. Additionally, the effect of nanoparticle concentration remained unclear: While some studies show improvements of mechanical properties at 0.1 vol%,[43] others observe property degradation above 1.0 vol%[44] due to agglomeration or processing defects.

This study tests the hypothesis that laser-generated ZrO_2 nanoparticles, characterized by their narrow size distribution and high phase uniformity, offer more homogeneous dispersion and mechanical performance than chemically synthesized counterparts. To verify this, a controlled comparison is conducted using Fe20Cr samples additivated with each 0.1 or 1.0 vol% of the respective nanoparticle type (**Figure 1**). All samples are produced via PBF-LB/M under comparable processing conditions.

Before processing, ONPs are characterized by scanning electron microscopy (SEM), transmission electron microscopy (TEM), and TEM energy-dispersive X-ray spectroscopy (EDS). Their surface distribution on the powder is analyzed by SEM and SEM-EDS. After PBF-LB/M processing, SEM, SEM electron backscatter diffraction (EBSD), and electron channeling contrast imaging (ECCI) are used to assess microstructure and ONP retention. Mechanical performance is evaluated via hot-hardness, compression, and preliminary creep tests at 600 °C. This temperature corresponds to 0.49 Tm for Fe20Cr (Tm = 1515 °C) and is relevant within the industrial secondary creep regime.[45] This approach allows for a direct, quantifiable comparison of key material properties, considering both the nanoparticle synthesis method and dispersion, while offering insights into the associated strengthening mechanisms.

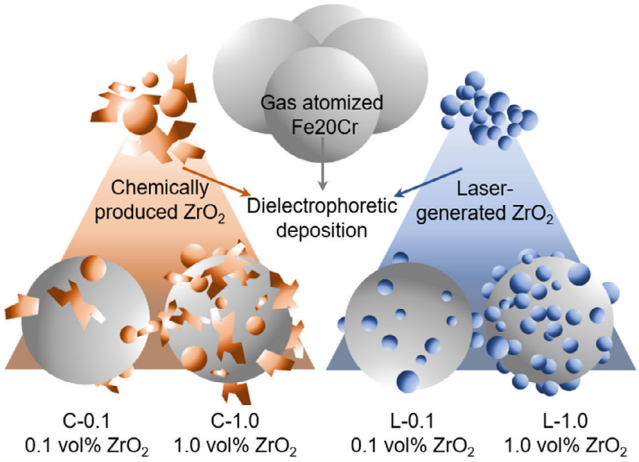

Figure 1. Visualization of ODS powder production routes and produced variants applied in this study.

2. Experimental Section

2.1. Materials

Laser-generated zirconia ONPs were synthesized from Zr700 material (VDM Metals, Altona, Germany) using LAL in deionized (DI) water (Figure 1). The composition of the target material, as characterized by X-ray fluorescence (XRF), revealed a composition of 98.70 wt% Zirconium (Zr), 1.23 wt% Hf, and a residual 0.07 wt% of trace elements. The conventional ONPs were produced using a chemical synthesis process, with a nominal average particle size provided by the supplier (abcr GmbH, Karlsruhe, Germany) of 20 nm and a composition of 99.9 wt% ZrO_2. The following size distribution information was determined: $D_{90} = 1257$ nm, $D_{50} = 26$ nm, and $D_{10} = 11$ nm. The metal base powder had a nominal composition of Fe20Cr (wt%). The initial particle size distribution provided by the manufacturer (Rosswag GmbH, Pfinztal, Germany) ranged from 15 to 45 µm ($D_{10} = 19$ µm, $D_{50} = 29$ µm, and $D_{90} = 43$ µm). XRF analysis confirmed the chemical composition of the Fe20Cr powder as 78.7Fe-21.2Cr (wt%).

2.2. Processing

2.2.1. Nanoparticle Synthesis by LAL

Laser-generated ONPs (L-ONPs) were produced by LAL to ensure precise control over ONP size and distribution.[16,46]

A focused laser beam targets the Zr700 material submerged in DI water, as described in a previous study.[19] For this study, a YLPN-0.5–1 × 5–80 ytterbium pulsed fiber laser (IPG Laser GmbH & Co. KG, Burbach, Germany) operates at 61 W, with a repetition rate of 3 MHz, a wavelength of 1064 nm, and a pulse duration of 1 ns. The laser beam was focused using an f/θ lens with a focal distance of 167 mm, resulting in a laser spot diameter of 40 µm. A spiral scanning pattern facilitated ablation, controlled by a MINISCAN III-14 galvanometric scanning unit (Raylase GmbH, Weßling, Germany). A peristaltic pump (LabV3, Baoding Shenchen Precision Pump Co., Ltd., Baoding, China) ensured a constant flow of DI water at 150 mL min^{-1} during the ablation procedure.

2.2.2. Dielectrophoretic Deposition of Nanoparticle-Additivated Metallic Powders

The dielectrophoretic deposition (DD) process[47,48] was used to produce ZrO_2-additivated Fe20Cr metallic powder by combining either chemically produced (C) or laser-generated ZrO_2 (L) ONPs with Fe20Cr powder. For each powder batch produced via DD, 496 g of Fe20Cr metal powder and 4 g of ZrO_2 ONPs (1.0 vol%; 0.8 wt% ZrO_2) or 499.6 and 0.4 g ZrO_2 ONPs (0.1 vol%; 0.08 wt% ZrO_2) were mixed with 300 mL DI water in a 2000 mL flask (Heidolph Scientific Products GmbH, Schwabach, Germany) as described in ref. [49].

2.2.3. AM by PBF-LB/M

The base and ONP-additivated Fe20Cr powders (Figure 1) were processed using a laboratory-scale PBF-LB/M system (Aconity MINI, Aconity3D GmbH, Germany). A Ytterbium fiber laser ($\lambda = 1064$ nm, spot diameter = 48 µm) was applied under an inert argon atmosphere (Ar 4.6, 1050 mbar), and the samples were produced on a 1.4404 (AISI 316 L) substrate. Processing parameters were optimized in preliminary trials to achieve maximum densification across all powder types. A constant hatch distance of 80 µm, a layer height of 30 µm, and a coater speed of 150 mm s^{-1} were used. Scan strategies included full-area exposure and interlayer rotation of 17°. Laser power (175–220 W) and scan speed (700–800 mm s^{-1}) were adjusted depending on the powder's optical absorption, which is influenced by nanoparticle type and concentration. The selected parameters are detailed in Table S1, Supporting Information. To ensure comparability, all samples were processed under parameter sets, resulting in a relative density of at least 99%, thereby minimizing processing-related variability.

2.2.4. Heat Treatment

After the PBF-LB/M process, selected as-built (AB) samples underwent heat treatment (HT). Solution annealing at 1100 °C for 1 h in an argon atmosphere, followed by air cooling, was chosen to mitigate the effects of rapid solidification and cooling inherent to the PBF-LB/M process.[50,51]

2.3. Analytical Methods

2.3.1. Nanoparticle Size and Chemical Composition Investigated by TEM and SEM

The ONPs were analyzed using TEM and SEM. TEM analysis was performed with a JEM-2200FS (JEOL GmbH, Freising, Germany) and SEM with Apreo S LoVac (Thermo Fisher Scientific GmbH, Schwerte, Germany). The size distribution of the ONPs was determined through image analysis of bright-field TEM and SEM images using ImageJ (Version 1.53 t). Smaller particles (<50 nm) were analyzed using TEM, capturing 594 particles for the L-ONPs. Contrary to the manufacturer's specified size range of ≈20 nm, a significant portion of the chemically produced ONPs (C-ONPs) was found to be in the micrometer range. Due to their unexpectedly large size, 110 particles were additionally characterized by SEM. In contrast, the L-ONPs were analyzed only using TEM images. TEM-EDS line scans were conducted to determine the chemical composition of ONPs. The acceleration voltages used for TEM images in this study were 200 and 5 kV for SEM.

2.3.2. Nanoparticle Crystal Structure Investigated by XRD

X-ray diffraction (XRD) was used to characterize the phase composition of the dry ONPs. This analysis utilized a D8 Advanced system (Bruker Corporation, Billerica, USA), operating in a Bragg–Brentano setup and emitting Cu Kα radiation (wavelength: 1.5406 Å). The XRD pattern was recorded in the 20°–70° 2θ range with a step size of 0.01° and an acquisition time of 5 s per step. The resulting diffractogram was analyzed using the DIFFRAC.EVA software (version 3.0).

2.3.3. Chemical Composition Analysis of Powder and Bulk Samples

The base and ZrO_2 ONP-additivated Fe20Cr powders and PBF-LB/M AB samples were analyzed for elemental composition using X-Ray Flourescence (XRF) with an S8 Tiger instrument (Bruker Corporation, Billerica, USA). The detection depths of ≈350 µm for powders and 45 µm for bulk samples confirm the reliability of XRF measurements for both material states. This instrument, equipped with a rhodium X-ray tube and a beryllium window, was operated at 4 kW. Powder samples (3 g) and cross-sections of AB cubic samples (region of interest (ROI): 8 mm diameter) were measured using the Quant-Express method to determine elemental weight percentages (wt%).

2.3.4. Microstructural Analysis of as- built Samples

Cross sections of AB base and ONP-additivated Fe20Cr samples were prepared metallographically for microstructural characterization. Densities were determined using optical microscopy (LOM, Leica DM-2700) and analyzed with ImageJ (version 1.53t) based on binarized porosity. For EBSD, samples were polished to a 1 µm finish, followed by OPS polishing and ultrasonic cleaning in ethanol for 10 min. EBSD data, collected using a Zeiss Sigma SEM (Carl Zeiss Microscopy GmbH, Jena,

Germany) and a Nordlys Nano detector (Oxford Instruments Co., Ltd., Oxford, UK), were processed with the AZtecCrystal software to generate inverse pole figure maps.

To preserve ONP morphology and evaluate particle retention, high-resolution SEM (Helios G5) imaging was conducted on OPS-polished surfaces. ImageJ (v1.54j) and Python libraries (Pandas, Numpy, Matplotlib) were used to determine ONP size, count, and interparticle distance (IPD); the analysis script is available in the Supplementary Information (Methods S1, Supporting Information). Further characterization was performed using FIB-SEM (Zeiss XB 550 L, Carl Zeiss Microscopy Deutschland GmbH, Oberkochen, Germany) and ECCI at 20 kV and a working distance of 6–7 mm to detect ONPs, including subsurface features. Atomic force microscopy (AFM) (LiteScope, Nenovision, Brno, Czech Republic) was used to validate the ECCI findings and distinguish ONPs from pores or preparation artifacts.

2.4. Mechanical Testing

2.4.1. Hot-Hardness Measurements of Bulk Samples

AB and HT specimens were prepared for hardness testing through standard metallographic grinding and polishing to a 1 µm finish. Vickers hardness was measured using an SRV 4 (Optimol Instruments Prüftechnik GmbH, Munich, Germany) tribometer equipped with a high-temperature heating module. Tests were conducted at room temperature (RT) of 25, 400, and 600 °C under a 9.81 N load (HV1) in an argon atmosphere to prevent oxidation. A heating rate of $10\,K\,s^{-1}$ and a dwell time of 15 min ensured thermal consistency while minimizing microstructural changes. Fifteen indentations were performed at each temperature, and the results were averaged. Indentations were analyzed at room temperature (RT) using optical microscopy.

2.4.2. High-Temperature Compression Testing of PBF-LB/M Samples

Cylindrical samples (5 mm diameter, 14 mm height) were produced via PBF-LB/M using the parameters in Table S1, Supporting Information, and cut from the substrate plate. HT samples were machined to a diameter of 4 mm and a length of 6 mm. Compression tests were performed in a DIL805 dilatometer (TA Instruments, New Castle, USA) under vacuum, with induction heating raising the temperature to 600 °C within 2 min. Samples were compressed at a strain rate of $0.0017\,s^{-1}$ to 25% deformation, followed by 3 min cooling. Actual stress (σ_{true}) and true strain (ε_{true}) were derived from load-displacement data, and the 0.2%-offset method was used to determine the flow stress (σ_f), indicating the onset of plastic deformation.

2.4.3. High-Temperature Creep Testing of PBF-LB/M Samples

To evaluate the long-term mechanical stability of the PBF-LB/M samples, preliminary uniaxial compression creep tests were conducted on selected HT samples. Cylindrical specimens (4 mm diameter, 6 mm height) were machined in the same way as for compression testing. Tests were performed at 600 °C under 50 MPa using a 12 kN creep frame with a three-zone furnace. Temperature was controlled via a thermocouple near the sample center, and axial strain was continuously recorded with an inductive sensor (DK25NLR5, WayCon, Brühl, Germany). Each test ran for 2 weeks.

3. Results and Discussion

3.1. Comparison of NP Chemistry and Morphology

In **Figure 2**, C- and L-ONPs are compared in terms of morphology, shape, and crystal structure and analyzed using SEM (Figure 2a), TEM (Figure 2d), TEM-EDS (Figure 2b,e), and XRD (Figure 2c,f). Quantitative particle size data derived from these methods are summarized in Table S2, Supporting Information.

The C-ONPs (Figure 2a) show a broad size distribution ranging from nanometers to micrometer-sized dendritic structures ($D_{90} = 1257$ nm and $D_{10} = 11$ nm). This inhomogeneity is attributed to uncontrolled nucleation and growth during synthesis, likely influenced by oversaturation and growth-directing anions such as chlorides or hydroxides.[52–54] Although uniform synthesis of particles smaller than 30 nm is reported,[55,56] such consistency was not achieved under the present synthesis route.

In contrast, L-ONPs (Figure 2d) exhibit a narrow size distribution ($D_{90} = 10$ nm and $D_{10} = 3$ nm) and predominantly spherical morphology. The observed uniformity is a direct consequence of the rapid cooling and surface tension effects inherent to LAL.[57–59] No agglomerates or oversized particles were observed in SEM or TEM imaging. For size analysis, more than 500 individual particles were evaluated using high-resolution TEM at varying magnifications. Figure 2d provides an overview and includes representative particle clusters; quantitative measurements were based on isolated ONPs.

Elemental compositions determined by TEM-EDS (Figure 2b,e) confirm Zr and O as primary constituents in both ONP types. L-ONPs (72 at% O, 28 at% Zr; 31 wt% O, and 69 wt% Zr) showed atomic ratios closer to stoichiometric ZrO_2 (67 at% O, 33 at% Zr; 26 wt% O, and 74 wt% Zr), while the C-ONPs (36 at% O, 37 at% Zr; 23 wt% O, and 77 wt% Zr) deviated slightly, possibly due to precursor residues or surface adsorbates.

XRD analysis (Figure 2c,f) revealed phase differences between both nanoparticle types. C-ONPs crystallized in the monoclinic ZrO_2 structure, whereas L-ONPs predominantly exhibited a tetragonal phase, with minor HfO_2 traces originating from the ablation target.

These results highlight substantial differences in particle size, morphology, and phase composition. While more than 500 L-ONPs were statistically analyzed, the irregular shape and clustering of C-ONPs limited the dataset to 30 well-resolved particles, as observed in SEM, supplemented by TEM data for broader representation. Despite this, the data provide a robust basis for evaluating the influence of ONP characteristics on microstructure and mechanical performance, which is explored in the following sections.

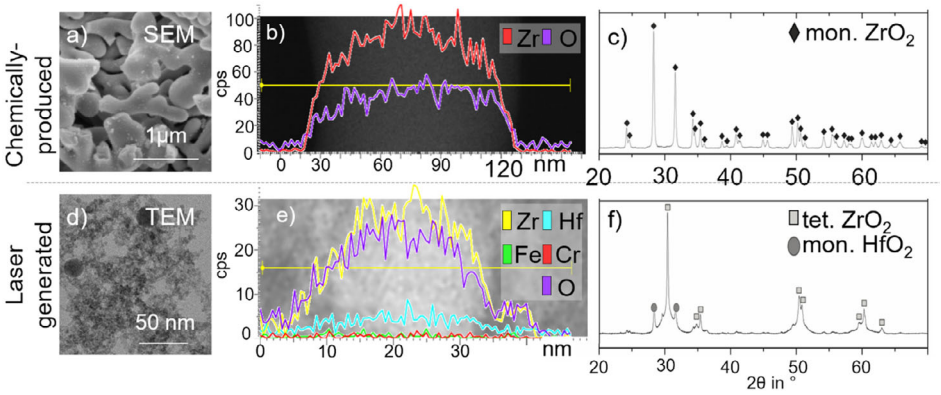

Figure 2. a) SEM, d) TEM, b,e) TEM-EDS line scans, and c,f) XRD of a–c) C-ONPs and d–f) L-ONPs.

3.2. Influence of NP Loading and Type on the NP Distribution on ODS Powders

In **Figure 3**, a SEM and SEM-EDS comparison of the spatial distribution of C-and L-ZrO_2 ONPs on Fe20Cr microparticles is shown. Quantitative elemental data are provided in Table S3, Supporting Information.

C-ONPs (Figure 3j,h) tend to form large agglomerates (≥500 nm), reflecting their irregular, dendritic morphology. In contrast, L-ONPs (Figure 3n,r,t) form smaller, more uniform clusters (<100 nm) with more homogeneous surface coverage. This is attributed to their narrower size distribution and spherical shape. Despite their nanoscale uniformity, even L-ONPs exhibit some agglomeration due to van der Waals forces and surface energy effects.[60] Higher ONP loading increases the frequency and size of agglomerates in both systems. However, at 1.0 vol% addition, L-ONPs create a more continuous and homogeneous coating layer (Figure 3r), while C-ONPs leave visibly uncovered regions at 0.1 vol% (Figure 3j).

While this trend is consistent across the series, the number of visually distinguishable ONPs may appear lower in some laser-modified samples (e.g., Figure 3s,r) compared to chemically modified ones (e.g., Figure 3k,j), despite the higher loading. This is attributed to the small size and dense surface coverage of L-ONPs, which, at sufficient concentration, form a near-continuous nanolayer that appears uniform in SEM imaging. Additionally, these particles' low electrical conductivity and minimal volume reduce contrast in electron imaging, making them less distinguishable than the larger, topographically protruding C-ONPs. We have clarified this optical effect in the manuscript to avoid potential misinterpretation of the particle distribution behavior.

XRF analysis (**Figure 4**) complements SEM-EDS by providing bulk quantification of Zr. EDS, with its shallow penetration depth, is particularly sensitive to compositional variations at the particle surface, where clustered ONPs were visually observed in SEM images (see Figure 3j). Therefore, higher Zr readings in chemically modified powders may partly reflect the presence of loosely adhered ONP clusters on the powder surface. Conversely, L-ONPs yield lower but more uniform Zr signals in both EDS and XRF, supporting the visual impression of even distribution. It is worth noting that EDS measurements on powder surfaces are influenced by surface roughness, particle curvature, and potential charging effects, which can contribute to signal variability and quantification uncertainty.[61]

Theoretical Zr contents for 0.1 and 1.0 vol% additions are ≈0.06 and 0.6 wt%, respectively. However, both EDS and XRF measurements show sublinear increases with higher ONP loading. This deviation indicates a saturation limit for ONP adherence to the powder surface, with excess particles likely detaching during mixing or handling. These findings highlight the more homogeneous distribution characteristics of L-ONPs and establish a compositional basis for evaluating their retention and mechanical impact, which will be discussed in the following sections.

3.3. Influence of ODS Powders on the Microstructure of PBF-LB/M Processed Parts

In the cross-sectional images (**Figure 5**), it can be seen that the addition of ONPs alters both porosity and pore morphology in Fe20Cr samples. The non-additivated reference (Figure 5a) exhibits the highest density (99.98%) with isolated spherical pores, typically associated with gas entrapment. In contrast, samples with 1.0 vol% ONPs exhibit a density reduction down to 99.04% and irregular dark features. Although similar features have been described as slag inclusions in Al-containing steels,[40–42] no reactive alloying elements or internal structures were detected here. Thus, these defects are attributed to incomplete ONP incorporation and were included in the densification analysis as pore-like features.

While the absolute change in density is small (e.g., 99.98–99.04%), such differences may significantly impact creep performance. Previous studies on AM 316 L have shown that even a porosity of ≈0.1% can reduce creep life due to cavity nucleation at defects.[62]

HT at 1100 °C for 1 h did not change porosity but significantly affected the microstructure. The EBSD images (**Figure 6**) illustrate the grain structures of the studied samples. The reference material (Figure 6i,j) exhibits the expected ferritic grain structure typical of additively manufactured steels, with grain sizes (GSs) of no clear preferred direction and a size of 17 µm in the AB and 10 µm in the HT condition.

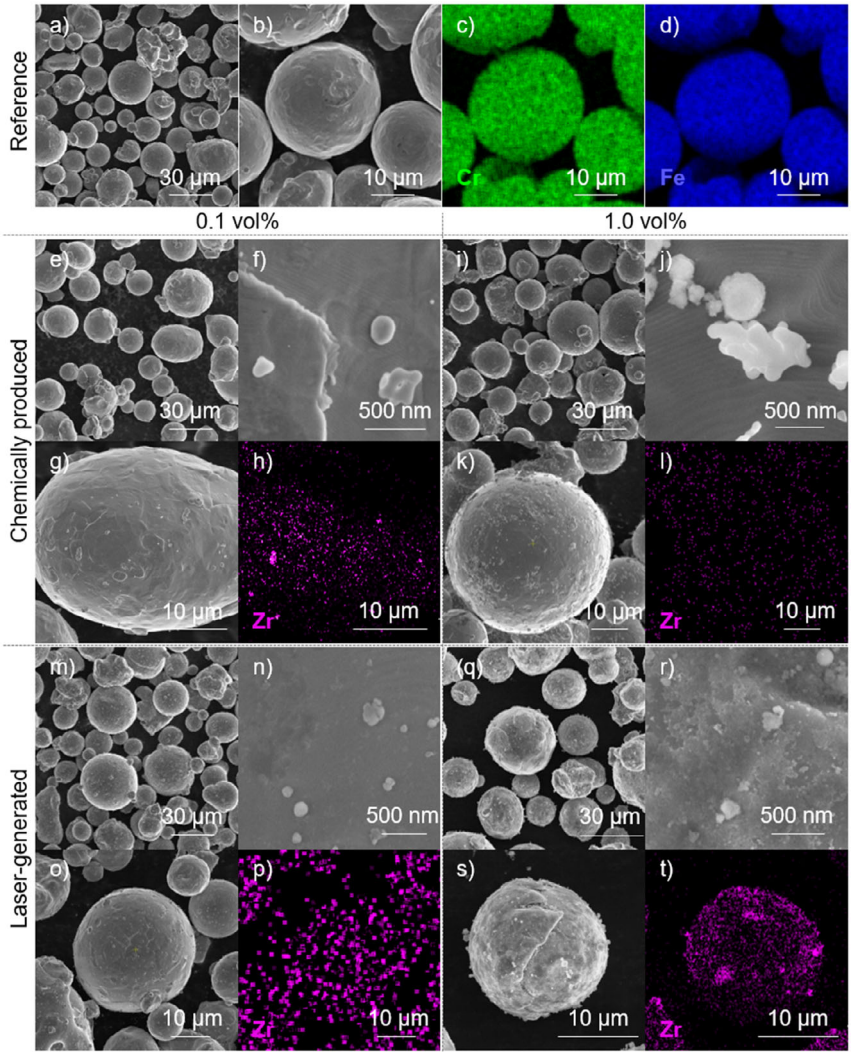

Figure 3. a,b,e–g,i–k,m–o,q–s) SEM imaging and c,d,h,l,p,t) SEM-EDS analysis of non-additivated Fe20Cr powder (upper section), chemically produced (middle section), and laser-generated (lower section) ZrO_2 NP distribution on Fe20Cr microparticles with 0.1 vol% (left) and 1.0 vol% (right) after feedstock additivation.

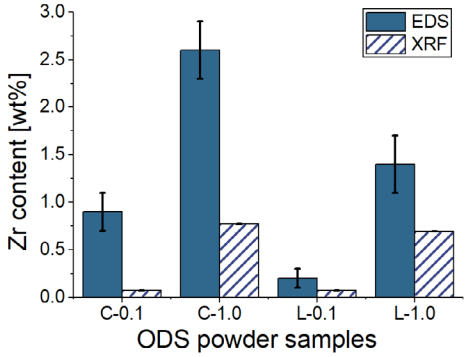

Figure 4. Zr content in the ODS powder as determined by EDS and XRF.

The rapid temperature fluctuations in the PBF process may lead to interrupted recrystallization, promoting a finer grain structure rather than grain coarsening. The nanoparticles act as grain growth barriers (Zener pinning), stabilizing this microstructure and favoring grain refinement. The recrystallization process during HT is initiated by heating the ferrite to a specific temperature range (<700–1300 °C[63–65]), where the thermal energy provided allows grains to overcome nanoparticle pinning. At higher temperatures, grains gain sufficient energy to coarsen by bypassing the particles, leading to grain growth and forming a new, more homogeneous grain structure.[66]

Samples with L-ONPs (Figure 6c,d) initially (AB) exhibit a visibly higher number of very fine grains than those with C-ONPs, yet no measurable anisotropy is observed. In contrast, the heat-treated L-0.1/1.0 (Figure 6g,h) samples are the only ones to show distinct anisotropy, with grains aligned along the build direction (BD) and aspect ratios (vertical mean linear intercept (MLI)/horizontal MLI) of 2.03 ± 1.46 (L-0.1) and 2.80 ± 2.25 (L-1.0), respectively. In contrast, samples with C-ONPs show no preferred grain elongation, neither in AB (Figure 6a,b) nor in HT (Figure 6e,f) condition, with aspect ratios close to 1.0.

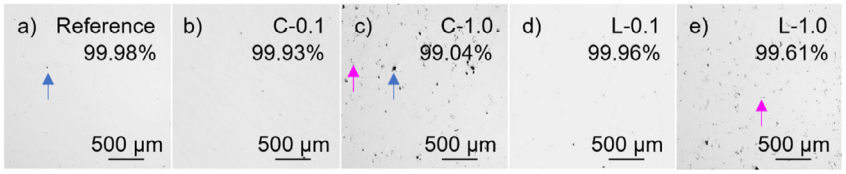

Figure 5. LOM images and part densities of PBF-LB/M samples in AB condition. Cross-sections show samples processed with a) no ONPs (reference), chemically synthesized ONPs at b) 0.1 vol% and c) 1.0 vol%, as well as d) laser-generated ONPs at 0.1 vol%, and e) 1.0 vol% loading.

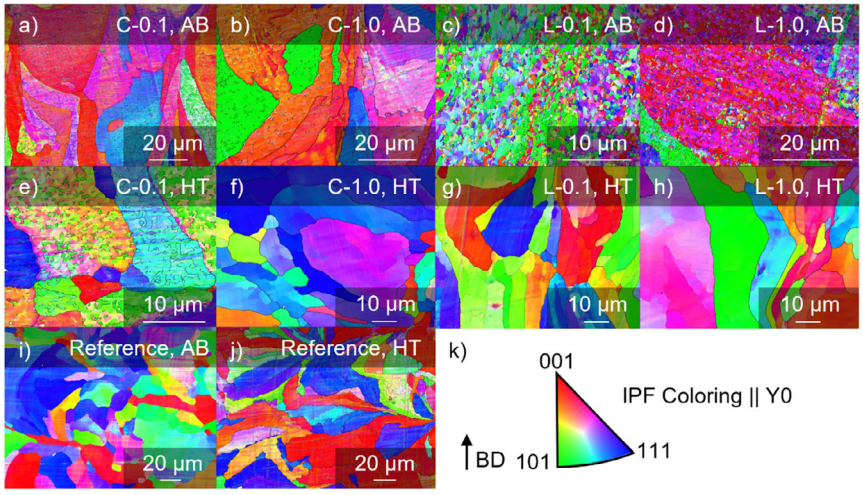

Figure 6. EBSD results of AB and HT ODS steel samples with a–j) representing IPF color maps according to the key depicted and BD in (k). C and L indicate samples with chemically (C) and laser-generated (L) ONP, respectively, while 0.1 and 1.0 represent the ONP volume fractions. The reference samples ((i) and (j)) highlight grain structures without ONPs in the AB and HT conditions.

The diagram in **Figure 7** quantifies these trends and confirms that ONP type and distribution influence GS evolution. The pronounced grain refinement observed in the AB condition for L-ONPs (GS ≈1 µm) is attributed to their small size and uniform dispersion, which enables effective grain boundary pinning during the cyclic thermal exposure of the PBF process. In contrast, the GS of C-0.1 decreases from 5 µm (AB) to 1 µm after HT, representing a 72% reduction. This may result from particle-stimulated nucleation at larger ONPs, due to their higher lattice mismatch and stronger interface energy. However, whether true nucleation or incomplete recrystallization, the underlying mechanism is not conclusively identified and may depend strongly on local processing and HT conditions. Both systems exhibit reduced refinement effects at higher ONP loadings (1.0 vol%), with GSs increasing to 16 µm for L-0.1 and 25 µm for L-1.0 after HT, likely due to particle agglomeration and coarsening.

While the EBSD data confirm general trends, the limited scan area may not capture all microstructural variability, particularly after HT. Additionally, exploring a broader temperature and duration range for HT would be valuable for optimizing and better understanding temperature-dependent changes in microstructural and mechanical alloy properties.

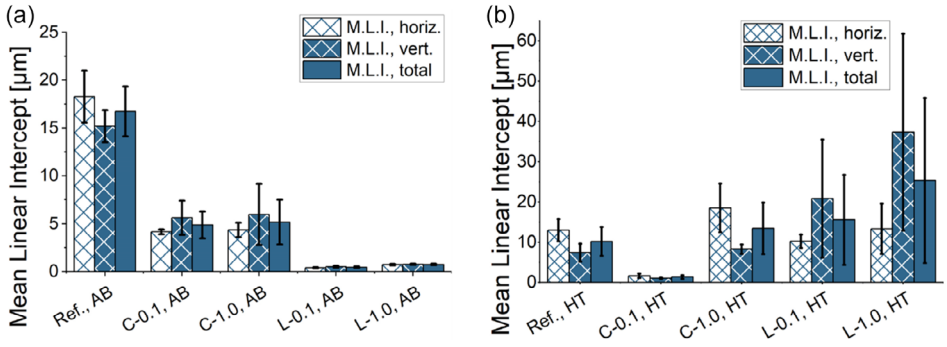

Figure 7. GSs determined by line intersection on the EBSD images in horizontal, vertical alignment to the build direction resulting in mean GS (total) calculated via MLI of the PBF-LB/M samples in a) AB and b) HT conditions.

3.4. Evaluation of NP Size and Distribution in PBF-LB/M Processed Parts

In XRF measurements (**Figure 8**), a marked reduction in Zr content is observed in as-built parts compared to the powder feedstocks, indicating nanoparticle loss during PBF-LB/M. The complete dataset is available in Table S4, Supporting Information. This loss, attributed to evaporation or spatter-induced ejection under high-temperature laser exposure, is more pronounced at higher ONP loadings. Quantitatively, C-ONPs exhibit 30% loss at 0.1 vol% and 25% at 1.0 vol%, whereas L-ONPs show 20% loss at 0.1 vol% and 30% at 1.0 vol%.

This loss can be attributed to particle evaporation or ejection during laser exposure. The elevated thermal input and interaction with process gas flows promote spatter and vaporization, especially for particles loosely bound at the surface. L-ONPs, although initially more homogenous dispersed, and smaller in size, become increasingly prone to loss at higher ONP loadings. This is explained by their tendency to coalesce during heating, which reduces surface area and weakens van der Waals interactions with the surrounding matrix. As a result, adhesion is reduced, and particles are more readily displaced or vaporized during melting.

At lower loadings, L-ONPs benefit from their high surface-to-volume ratio and stronger van der Waals forces, which promote higher adherence to the melt pool and result in lower loss rates compared to the bigger chemically synthesized counterparts. However, at higher ONP loadings, this advantage is negated by increased coalescence and a higher statistical probability of surface exposure to the laser, both of which amplify the risk of ejection or vaporization.

In contrast, C-ONPs—despite their larger size and less uniform distribution—are less prone to thermal coalescence, which may partially explain their more consistent retention behavior across different ONP loadings.

It should be noted that while matrix elements such as chromium are also subject to partial evaporation under PBF-LB/M conditions, they remain primarily embedded within the melt pool and benefit from rapid re-solidification. ONPs, particularly those at or near the surface or loosely present within the powder bed, experience weaker thermal coupling and are more vulnerable to localized overheating, recoil pressure, and gas flow-induced displacement. This makes their retention behavior fundamentally different and more prone to loss, despite the high thermal stability of ZrO_2 itself.

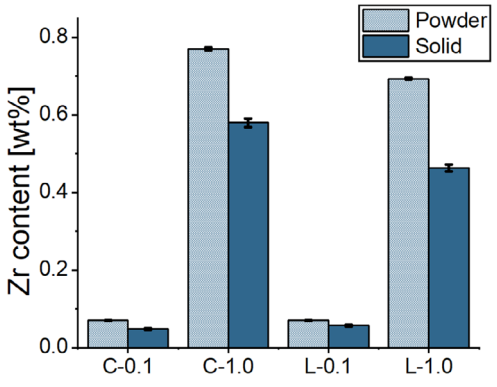

Figure 8. Measured Zr amounts (wt.-%) in the ODS powder feedstocks and AB PBF-LB/M ODS parts via XRF technique.

While XRF provides bulk data, its limited spatial resolution necessitates the use of complementary nanoscale techniques. ECCI imaging (**Figure 9**) reveals ONPs as nanoscale black dots (exemplary dashed with white circles), which AFM confirms as topographical protrusions with a height of ≈0.5–1 nm and a lateral size of 20–40 nm (Figure 9f–i), consistent with the expected ONP dimensions (**Figure 10**).

The yellow arrows indicate ONPs aligned along small-angle grain boundaries, supporting their role as pinning agents stabilizing the microstructure. Magenta arrows mark blurred ONPs beneath the surface, indicating sub-surface disruptions. Red arrows in Figure 9d and the zoomed view in Figure 9e highlight line-like features observed in the L-1.0 sample. Based on their morphology and location, they are interpreted as dislocation lines, in line with previous observations in similar ODS steels.[67–69] Their proximity to ONPs suggests a possible interaction, such as dislocation pinning or stress-induced formation from sample preparation. One potential cause may be internal stresses associated with the tetragonal-to-monoclinic phase transformation of L-ONPs during cooling (970–750 °C).[70] Further high-resolution investigations, such as TEM or HR-EBSD, would be required to confirm the exact mechanism.

The total number of ONPs detectable via ECCI varies significantly: L-1.0 yielded only 107 particles due to either image resolution or agglomeration-induced detectability loss. Representative high-magnification ECCI images used for particle size analysis are provided in Figure S1, Supporting Information, to illustrate the resolution and measurement basis. The ONP size distribution in bulk samples (Figure 10) shows that L-1.0 contains the largest ONPs, indicating coalescence. In contrast, C-0.1 exhibits the most petite average ONP sizes and the most uniform distribution.

SEM imaging (**Figure 11**) complements ECCI by enabling broader field analysis. ONPs appear as bright dots; however, particle sizes are generally overestimated due to charging and potential artifacts from sample preparation. However, larger particle sizes observed in SEM may indicate agglomeration behavior. For example, in Figure 11d, a spherical L-ONP with an approximate size of 70 nm can be observed, suggesting that ONPs may have undergone partial melting during the PBF-LB/M process, resulting in larger spherical volumes upon solidification. Furthermore, agglomerated ONPs are frequently observed in high-loading samples, forming dendritic structures (Figure 11i,j). In C-ONPs, larger particles retain their shape. They are found at the edges of these structures (Figure 11i), whereas L-ONPs (Figure 11j) appear to have melted together, contributing to the dendritic formation.

The IPD analysis (Figure 11k, and Table S5, Supporting Information) further clarifies the dispersion behavior of ONPs in the PBF-LB/M samples. Notably, the L-1.0 sample—despite its high ONP loading—exhibits the largest average IPD (734 ± 475 nm). This contradicts the expected trend of decreasing IPD with increasing ONP concentration, suggesting a saturation threshold at which additional particles no longer improve dispersion but promote agglomeration and localized growth.

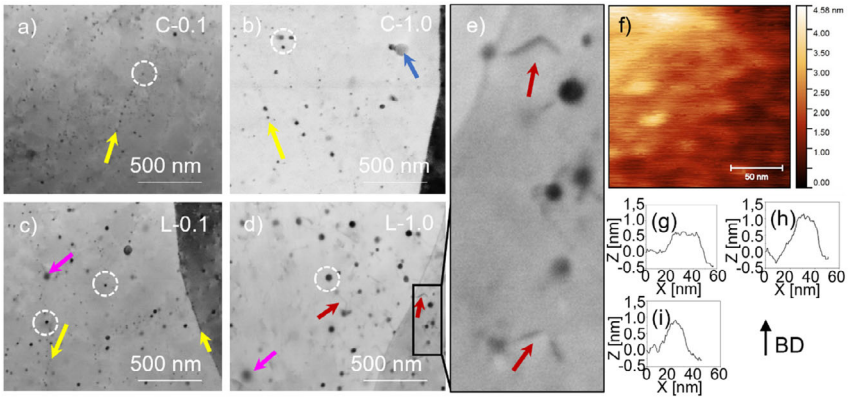

Figure 9. ECCI images of additivated solid samples with a,c) 0.1 vol% and b,d,e) 1.0 vol% a,b) C-ONPs and c–e) L-ONPs, exemplarily marked by the white dashed circles. Exemplary ONPs under the surface are shown with magenta arrows; dislocations are indicated with red arrows, and pores with blue arrows. f) AFM analyses with g–i) several measurements revealed elevations in the *Z*-direction.

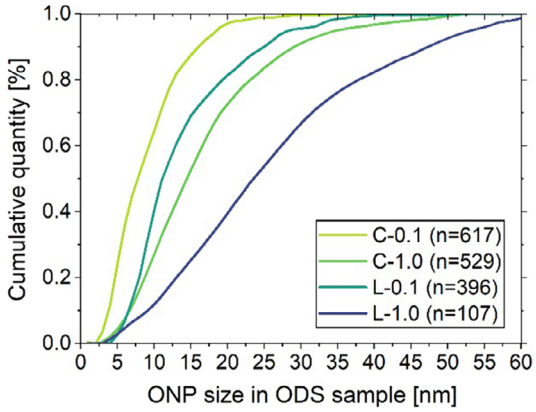

Figure 10. ONP size in PBF-LB/M processed samples in AB condition optically analyzed by ECCI images.

The reduced number of discrete particles in L-1.0 aligns with ECCI and SEM observations of particle clustering and coalescence.

In contrast, the low-loading L-sample (L-0.1) shows a lower average IPD, consistent with more effective dispersion and a higher number of individually detectable particles. For C-ONPs, the difference between C-0.1 (520 ± 348 nm) and C-1.0 (445 ± 309 nm) is less pronounced. Interestingly, C-1.0 exhibits a slightly smaller average IPD than C-0.1, despite its higher ONP loading. This is counterintuitive given that the C-0.1 sample contains the smallest ONPs (see Figure 10), which, under ideal dispersion, would be expected to produce the lowest IPD. One possible explanation lies in a less uniform particle distribution in C-0.1 or sampling limitations in the image-based evaluation. However, it may also reflect the lower tendency of C-ONPs to agglomerate under thermal exposure, as discussed in the XRF section. Unlike their laser-generated counterparts, the larger and structurally stable monoclinic ONPs exhibit reduced coalescence and stronger resistance to melt pool dynamics, potentially resulting in more consistent particle spacing even at higher loadings.

In summary, although L-ONPs exhibit a more homogenous initial dispersion and chemical purity, their tendency to agglomerate at higher ONP loadings reduces their effective particle number and dispersion quality postprocessing. This observation is crucial for evaluating the hypothesis that L-ONPs, if retained in a small, well-dispersed form, enhance strengthening efficiency through the Orowan mechanism.

3.5. Influence of NP Size and Distribution on Mechanical Properties of PBF-LB/M Processed Parts

The mechanical performance of PBF-LB/M-processed Fe20Cr samples was evaluated through hardness testing (RT, 400 °C, 600 °C) and compression tests at 600 °C, supported by creep experiments. The selected temperature of 600 °C corresponds to 0.49 Tm for Fe20Cr (Tm = 1515 °C) and lies within the secondary creep regime,[45] ensuring relevance for high-temperature applications.

In the AB condition (**Figure 12**a), the reference sample exhibited the highest hardness. All ONP-additivated samples showed slightly lower values, with L-1.0 (AB) marginally lower than the chemically modified variants. HT at 1100 °C for 1 h (Figure 12b) reduced the hardness across all samples due to recrystallization and grain growth (see Figure 6 and 7).

However, the extent of degradation varied depending on ONP type and loading. L-ONPs at 1.0 vol% (L-1.0, HT) achieved the highest hardness values (171 HV1 at RT and 168 HV1 at 400 °C), followed by C-1.0 (168 HV1 at RT and 156 HV1 at 400 °C), while 0.1 vol% ONP samples showed only minor improvements over the reference (150 HV1 at RT and 140 HV1 at 400 °C). The reduced variability observed in L-1.0 suggests a more homogeneous strengthening effect, consistent with homogeneous dispersion and finer ONP size. For comparison, in **Table 1**, the results of hardness measurements of HT samples at RT and 400 °C are shown.

Compression testing at 600 °C (Figure 12c) confirmed these trends and highlighted the influence of GS and IPD on the flow stress. C-0.1 exhibited the highest strength with an increase of 21% compared to the reference (252 ± 7 MPa), followed by

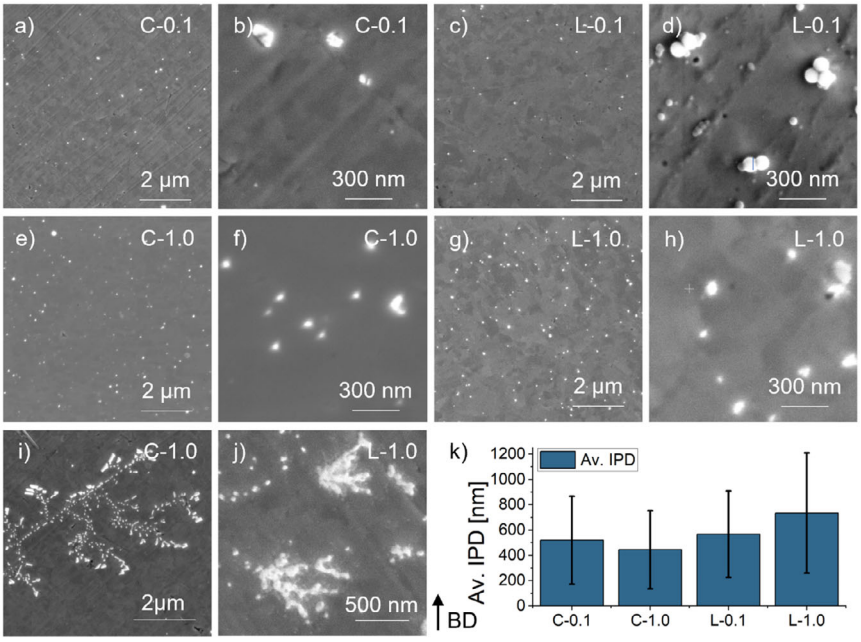

Figure 11. SEM images of additivated solid samples with a–d) 0.1 vol% and e–j) 1.0 vol% a,b,e,f,i) C-ONPs and c,d,g,h,j) L-ONPs in different magnifications. The optical analyzed IPD of the ODS samples is shown in diagram (k) with the values in Table S5, Supporting Information.

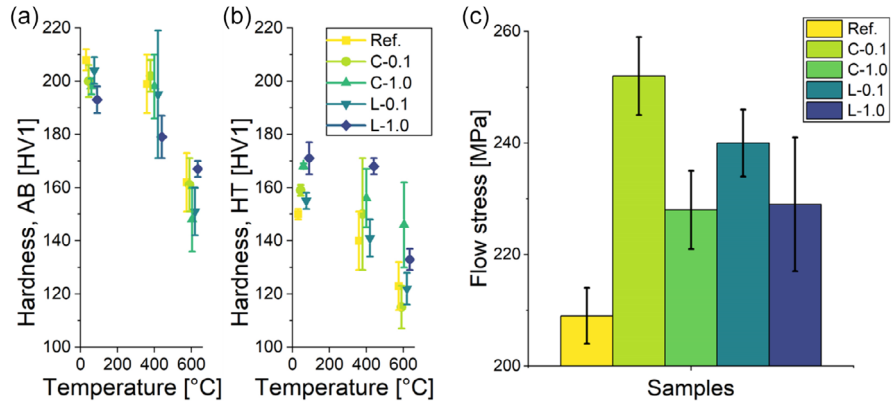

Figure 12. Hardness measured at room and elevated temperature on a) AB and b) HT parts, flow stress as a result of compression tests on c) HT parts at 600 °C.

Table 1. Vickers hardness of as-built parts at RT and 400 °C in HT condition.

	Vickers Hardness at RT	SD	Vickers Hardness at 400 °C	SD
	HV1	HV1	HV1	HV1
Ref, HT	150	2	140	11
L-0.1, HT	155	3	141	7
L-1.0, HT	171	6	168	3
C-0.1, HT	159	2	150	21
C-1.0, HT	168	1	156	11

15% for L-0.1 (240 ± 6 MPa), and ≈10% for C-1.0 (228 ± 7 MPa) and L-1.0 (229 ± 12 MPa). The high flow stress of C-0.1 correlates with its refined GS (1 ± 1 µm) and moderate IPD (520 ± 348 nm). In contrast, L-1.0, despite containing smaller ONPs, showed a lower flow stress due to a coarser GS (25 ± 21 µm) and the highest IPD (734 ± 475 nm). These findings indicate that GS primarily governs flow stress in short-term plastic deformation, while IPD plays a secondary role. ONP size alone is not decisive unless supported by practical grain refinement and dispersion.

In contrast, creep deformation at 600 °C and 50 MPa (**Figure 13**) was more strongly influenced by the ONP type

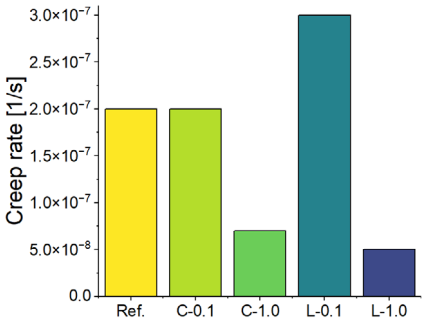

Figure 13. Results of creep tests performed at 600 °C under 50 MPa using a 12 kN creep frame (HT condition).

and ONP loading. The L-1.0 sample, characterized by the highest aspect ratio (2.80 ± 2.25), demonstrated the lowest steady-state creep rate ($5.0 \times 10^{-8}\,s^{-1}$), followed by C-1.0 ($7.0 \times 10^{-8}\,s^{-1}$), both significantly lower than the reference ($2.0 \times 10^{-7}\,s^{-1}$). The lowest result for L-1.0 in comparison to the other samples was confirmed by a repeat test, supporting the reliability of the observed lower creep rate. Although minor density variations might impact creep performance, as discussed earlier, such an effect was not prominently observed here.

C-0.1, despite achieving the highest flow stress, showed inferior creep resistance compared to higher ONP-loaded samples. This suggests the benefits of grain refinement diminish during prolonged thermal exposure. The notably poorer creep performance of L-0.1 ($3.0 \times 10^{-7}\,s^{-1}$) correlates with increased nanoparticle agglomeration, indicated by larger ONP sizes comparable to C-1.0 and a relatively high aspect ratio (2.03 ± 1.46). Such agglomerates likely reduce the efficiency of individual nanoparticles for Orowan-type dislocation pinning and introduce local structural imperfections, which may explain the observed differences.

To evaluate the potential influence of Zr content on the mechanical performance, the actual Zr concentrations in the printed parts were determined via XRF (Figure 8): L-0.1 = 0.057 wt%, C-0.1 = 0.048 wt%, L-1.0 = 0.463 wt%, and C-1.0 = 0.580 wt%. While C-1.0 exhibits the highest overall Zr content, the higher creep resistance and hot-hardness observed for L-1.0 suggest that total Zr content alone is not the dominant factor. Instead, particle size, dispersion quality (IPD), and microstructural stability play a more decisive role.

The mechanical response of the investigated ODS steels is thus governed by ONP load-specific mechanisms: GS and IPD dictate performance in short-term loading. At the same time, thermally stable dispersoids control long-term behavior. These findings confirm that L-ZrO_2 ONPs, when well-dispersed, are particularly effective in improving high-temperature creep resistance. However, their tendency to agglomerate at higher concentrations can lead to increased IPD and reduced strengthening efficiency.

It is important to note that the creep tests presented here were exploratory and based on single measurements per condition. While trends are observed, further replicates are needed to establish statistical robustness. Moreover, the selected creep temperature was chosen for consistency with compression testing and does not cover the full range of application-relevant conditions, which may involve higher temperatures and stresses.

Future studies should include post-mortem high-resolution analysis (e.g., TEM and HR-EBSD) to investigate dislocation–particle interactions and directly validate proposed mechanisms such as Orowan looping or particle pinning. Complementary chemical analysis may further elucidate the stability of ONP, potential interfacial reactions, and phase transformations under thermal exposure. These insights are crucial for optimizing ONP type, ONP loading, and processing parameters to achieve higher long-term performance in ODS steels.

4. Conclusions

This study demonstrates that the synthesis route and concentration of ZrO_2 nanoparticles significantly influence their distribution, microstructural integration, and strengthening mechanisms in PBF-LB/M-processed Fe20Cr ODS steels. L-ONPs, characterized by a narrow size distribution ($D_{90} = 10$ nm) and tetragonal phase composition, showed more homogeneous initial dispersion than chemically synthesized, polydisperse monoclinic ONPs ($D_{90} = 1257$ nm). However, at higher ONP loadings (1.0 vol%), L-ONPs exhibited coalescence and agglomeration, leading to an increased IPD (734 ± 475 nm) and reduced retention, as evidenced by XRF and ECCI.

The mechanical response depends on distinct microstructural factors. Compression strength at 600 °C correlated primarily with GS, with C-0.1 achieving the highest flow stress (252 ± 7 MPa) due to a refined GS (1 ± 1 µm) and moderate IPD (520 ± 348 nm). In contrast, creep resistance correlated more strongly with ONP loading, GS aspect ratio, and agglomeration tendencies rather than grain refinement alone. Specifically, the lowest creep rate ($5.0 \times 10^{-8}\,s^{-1}$ for L-1.0) corresponded to high ONP loading combined with elongated ONPs and minimal agglomeration, promoting effective Orowan pinning.

These results partially confirm the hypothesis that L-ONPs, characterized by narrow size distributions and high uniformity, can positively influence creep resistance. However, contrary to initial expectations, the advantage of L-ONPs is not consistent across all loadings. While L-1.0 exhibited superior creep performance, the unexpectedly poor creep resistance of L-0.1 indicates significant open questions regarding the impact of nanoparticle distribution and agglomeration. Such agglomeration appears to substantially reduce effective nanoparticle-based strengthening mechanisms, overshadowing potential advantages derived from their initial uniformity. In contrast, C-ONPs showed stable microstructural refinement and strengthening at lower concentrations.

Overall, the interplay between nanoparticle type, size, and dispersion determines the dominant strengthening mechanism. For short-term performance, grain refinement—achieved through small and well-distributed ONPs—is most effective. In contrast, long-term creep resistance correlates with a higher ONP loading and a homogeneous, finely dispersed distribution with minimal agglomeration. These insights provide a foundation for tailoring ONP synthesis and processing strategies to application-specific mechanical demands in ODS alloys.

Supporting Information

Supporting Information is available from the Wiley Online Library or from the author.

Acknowledgements

The authors thank Hamed Shokri and Michael Blüm for their preliminary work on the compression tests, as well as Jan Hendrik Vehrs for his contributions during his master's thesis. Thanks to Tobias Bochman and Matthias Epple for conducting the SEM/EDS (Faculty for Chemistry at University Duisburg Essen) analysis of the powder samples and Jonathan Edling's support in performing the hot-hardness measurements. Daniel Behrens is acknowledged for his support of the PBF-LB/M processing, and Johanna Dell'Anno is recognized for supporting the production of the laser-generated ONPs. The authors also thank Johannes Sailer for assisting with the evaluation of the compression tests. Salvatore Scrofani is credited for ECCI imaging, with additional contributions from Jan Goldberg and Kai Donnerbauer for in situ AFM. Parts of the text were linguistically refined with the assistance of OpenAI GPT-4. This research was conducted as part of the German Research Foundation (DFG) Priority Program 2122, "Materials for Additive Manufacturing" (SPP 2122, project number 493889809, GO 2566/13-1, and XU 121/20-1). Additionally, B. Gökce acknowledges support from the DFG Heisenberg Program, project GO 2566/10-1 (445127149). Marina Macias Barrientos thanks the DFG and the Ministerium für Kultur und Wissenschaft des Landes Nordrhein-Westfalen (MKW NRW, Ministry of Culture and Science of North Rhine-Westphalia) for their financial support within the Major Research Instrumentation Program (Focused Ion Beam Zeiss XB550 L (FIB-SEM, 386509496) and In-situ Atomic Force Microscope (445052562)).

Open Access funding enabled and organized by Projekt DEAL.

Conflict of Interest

The authors declare no conflict of interest.

Author Contributions

Mareen Goßling: conceptualization (equal); investigation (lead); validation (lead); visualization (lead); and writing—original draft (lead). **Silja-Katharina Rittinghaus**: conceptualization (equal); writing—original draft (supporting). **Felix Radtke**: investigation (supporting) and writing—original draft (supporting). **Abdelrahman Elsayed**: investigation: (supporting) and writing—original draft: (supporting). **Marina Macias Barrientos**: investigation (supporting) and writing—original draft (supporting). **Ulf Ziesing**: investigation (supporting) and writing—original draft (supporting). **Louis Becker**: investigation (supporting); validation (supporting); and writing—review and editing (supporting). **Ihsan Murat Kuşoğlu**: investigation (supporting) and writing—original draft (supporting). **Christoph Broeckmann**: funding acquisition (supporting) and supervision (supporting). **Ulrich Krupp**: funding acquisition (supporting) and supervision (supporting). **Avinash Hariharan**: writing—review and editing (supporting). **Sebastian Weber**: funding acquisition (supporting); validation (supporting); and writing—review and editing (supporting). **Bilal Gökce**: conceptualization (equal); funding acquisition (lead); and writing—review and editing (supporting).

Data Availability Statement

The data that support the findings of this study are available from the corresponding author upon reasonable request.

Keywords

high temperature, heat treatment strength, laser ablation in liquids, laser powder bed fusion, nanoparticles

Received: January 31, 2025
Revised: April 10, 2025
Published online: May 13, 2025

[1] S. Eswarappa Prameela, T. M. Pollock, D. Raabe, M. A. Meyers, A. Aitkaliyeva, K.-L. Chintersingh, Z. C. Cordero, L. Graham-Brady, *Nat. Rev. Mater.* **2023**, *8*, 81.
[2] Q. Li, C. M. Parish, K. A. Powers, M. K. Miller, *J. Nucl. Mater.* **2014**, *445*, 165.
[3] A. Wasilkowska, M. Bartsch, U. Messerschmidt, R. Herzog, A. Czyrska-Filemonowicz, *J. Mater. Process. Technol.* **2003**, *133*, 218.
[4] G. Gottstein, *Materialwissenschaft und Werkstofftechnik: Physikalische Grundlagen*, 4th ed., Springer Berlin Heidelberg, Berlin, Heidelberg **2014**, pp. 219–319.
[5] S. K. Karak, T. Chudoba, Z. Witczak, W. Lojkowski, I. Manna, *Mater. Sci. Eng. A* **2011**, *528*, 7475.
[6] C. Capdevila, M. K. Miller, K. F. Russell, J. Chao, J. L. González-Carrasco, *Mater. Sci. Eng. A* **2008**, *490*, 277.
[7] I. Hilger, X. Boulnat, J. Hoffmann, C. Testani, F. Bergner, Y. Carlan, F. de Ferraro, A. Ulbricht, *J. Nucl. Mater.* **2016**, *472*, 206.
[8] S. Chung, B. Lee, S. Y. Lee, C. Do, H. J. Ryu, *J. Mater. Sci. Technol.* **2021**, *85*, 62.
[9] Y. Tang, S. Yang, Y. F. Zhao, in *Handbook of Sustainability in Additive Manufacturing* (Eds: S. S. Muthu, M. M. Savalani), Springer Singapore, Singapore **2016**, pp. 101–144.
[10] W. Liu, X. Liu, Y. Liu, J. Wang, S. Evans, M. Yang, *Sustainability* **2023**, *15*, 3827.
[11] D. Gu, X. Shi, R. Poprawe, D. L. Bourell, R. Setchi, J. Zhu, *Science* **2021**, *372*, eabg1487.
[12] M. A. Meyers, K. K. Chawla, in *Mechanical Behavior of Materials*, Cambridge University Press, Cambridge **2012**.
[13] D. Pilone, G. Pulci, L. Paglia, A. Mondal, F. Marra, F. Felli, A. Brotzu, *Metals* **2020**, *10*, 1457.
[14] H. Tang, X. Chen, M. Chen, L. Zuo, B. Hou, Z. Wang, *Mater. Sci. Eng. A* **2014**, *609*, 293.
[15] J. H. Schneibel, M. Heilmaier, W. Blum, G. Hasemann, T. Shanmugasundaram, *Acta Mater.* **2011**, *59*, 1300.
[16] D. Zhang, B. Gökce, S. Barcikowski, *Chem. Rev.* **2017**, *117*, 3990.
[17] A. Subhan, A.-H. I. Mourad, Y. Al-Douri, *Nanomaterials* **2022**, *12*, 8.
[18] S. Z. Mat Isa, R. Zainon, M. Tamal, *Materials* **2022**, *15*, 3.
[19] M. Goßling, S.-K. Rittinghaus, S. Bharech, Y. Yang, M. B. Wilms, L. Becker, S. Weber, B.-X. Xu, B. Gökce, *J. Mater. Res.* **2024**, *39*, 774.
[20] M.-H. Tsai, S.-Y. Chen, P. Shen, *J. Chem. Phys.* **2005**, *122*, 204708.
[21] D. Tan, Y. Teng, Y. Liu, Y. Zhuang, J. Qiu, *Chem. Lett.* **2009**, *38*, 1102.
[22] N. Bärsch, J. Jakobi, S. Weiler, S. Barcikowski, *Nanotechnology* **2009**, *20*, 445603.
[23] A. I. Kostyukov, A. A. Nashivochnikov, V. Snytnikov, M. I. Rakhmanova, V. N. Snytnikov, *Quantum Electron.* **2022**, *52*, 149.
[24] A. Adamski, P. Jakubus, Z. Sojka, *Nukleonika* **2006**, *51*, S27.
[25] C. Wang, *Ph.D. Thesis*, University of Stuttgart, Max Planck Institute for Metals Research, Stuttgart, Germany **2006**, pp. 5–6.
[26] Y. Kawasaki, Y. Ikeda, T. Kobayashi, H. Sumiyoshi, *ISIJ Int.* **1996**, *36*, 1208.
[27] N. Sekido, A. Hoshino, M. Fukuzaki, Y. Yamabe-Mitarai, T. Maruko, *Mater. Sci. Eng. A* **2011**, *528*, 8451.
[28] M. Silalahi, B. Bandriyana, S. Ahda, B. Sugeng, A. Dimyati, *J. Phys.: Conf. Ser.* **2020**, *1436*, 12055.

[29] L. L. Hsiung, HRTEM Study of Oxide Nanoparticles in Fe-16Cr ODS Ferritic Steel Developed for Fusion Energy, Lawrence Livermore National Laboratory, LLNL-BOOK-438635, June 25, **2010**.
[30] T. A. H. Nguyen, A. V. Nguyen, *Langmuir* **2012**, *28*, 16725.
[31] E. Homede, O. Manor, *J. Colloid Interface Sci.* **2020**, *562*, 102.
[32] T. Boegelein, E. Louvis, K. Dawson, G. J. Tatlock, A. R. Jones, *Mater. Charact.* **2016**, *112*, 30.
[33] L. L. Hsiung, M. J. Fluss, A. Kimura, *Mater. Lett.* **2010**, *64*, 1782.
[34] M. B. Wilms, S.-K. Rittinghaus, M. Goßling, B. Gökce, *Prog. Mater. Sci.* **2023**, *133*, 101049.
[35] Z. Li, Z. Lu, R. Xie, C. Lu, Y. Shi, C. Liu, *Fusion Eng. Des.* **2017**, *121*, 159.
[36] Q. Tang, T. Hoshino, S. Ukai, B. Leng, S. Hayashi, Y. Wang, *Alloys. Mater. Trans.* **2010**, *51*, 2019.
[37] G. Zhang, Z. Zhou, H. Sun, L. Zou, M. Wang, S. Li, *J. Nucl. Mater.* **2014**, *455*, 139.
[38] A. Karch, D. Sornin, F. Barcelo, S. Bosonnet, Y. Carlan, R. de, Logé, *J. Nucl. Mater.* **2015**, *459*, 53.
[39] R. Jarugula, S. Koppoju, R. Jeyaraam, S. Ganesh Sundara Raman, G. Sundararajan, *Mater. Sci. Eng. A* **2021**, *800*, 140343.
[40] W. Hou, T. Stubbs, L. DeBeer-Schmitt, Y.-T. Chang, M.-A. Charpagne, T. M. Smith, A. Huang, Z. C. Cordero, *Addit. Manuf.* **2024**, *96*, 104554.
[41] T. Stubbs, R. Hou, D. N. Leonard, L. DeBeer-Schmitt, Y. Zhu, Z. C. Cordero, A. Huang, *Addit. Manuf. Lett.* **2024**, *9*, 100195.
[42] C. Kenel, A. Luca, S. S. de, Joglekar, C. Leinenbach, D. C. Dunand, *Addit. Manuf.* **2021**, *47*, 102224.
[43] K. A. Unocic, B. A. Pint, D. T. Hoelzer, *J. Mater. Sci.* **2016**, *51*, 9190.
[44] A. Afandi, R. Nisa, K. A. Z. Thosin, *J. Phys.: Conf. Ser.* **2017**, *817*, 12028.
[45] A. P. Mouritz, in *Introduction to Aerospace Materials*, Elsevier, Amsterdam **2012**, pp. 521–533.
[46] I. Y. Khairani, G. Mínguez-Vega, C. Doñate-Buendía, B. Gökce, *Phys. Chem. Chem. Phys.* **2023**, *25*, 19380.
[47] R. Streubel, M. B. Wilms, C. Doñate-Buendía, A. Weisheit, S. Barcikowski, J. H. Schleifenbaum, B. Gökce, *Jpn. J. Appl. Phys.* **2018**, *57*, 40310.
[48] G. Marzun, C. Streich, S. Jendrzej, S. Barcikowski, P. Wagener, *Langmuir* **2014**, *30*, 11928.
[49] M. Goßling, S.-K. Rittinghaus, F. Radtke, A. Elsayed, I. M. Kusoglu, A. Hariharan, U. Krupp, B. Gökce, *Powder Metall.* **2024**, *30*.
[50] P. K. Parida, A. Dasgupta, S. K. Sinha, *J. Mater. Eng. Perform.* **2021**, *30*, 9227.
[51] H. Xu, Z. Lu, C. Jia, H. Gao, C. Liu, *High Temp. Mater. Processes* **2016**, *35*, 321.
[52] P. Stolzenburg, A. Freytag, N. C. Bigall, G. Garnweitner, *CrystEngComm* **2016**, *18*, 8396.
[53] F. Tana, A. Serafini, L. Lutterotti, A. Cigada, F. Variola, F. Bondioli, L. de Nardo, *CrystEngComm* **2018**, *20*, 879.
[54] W. Shao, G. Zangari, *J. Phys. Chem. C* **2009**, *113*, 10097.
[55] G. Shishodia, S. Gupta, N. Pahwa, P. K. Shishodia, *J. Electron. Mater.* **2024**, *53*, 5159.
[56] A. Behbahani, S. Rowshanzamir, A. Esmaeilifar, *Procedia Eng.* **2012**, *42*, 908.
[57] A. K. Mahmoud, Z. Fadhill, S. I. Al-nassar, F. I. Husein, E. Akman, A. Demir, *JMSE-B* **2013**, *3*.
[58] M. R. N. Soares, T. Holz, F. Oliveira, F. M. Costa, T. Monteiro, *RSC Adv.* **2015**, *5*, 20138.
[59] K. Choudhury, R. K. Singh, P. Kumar, M. Ranjan, A. Srivastava, A. Kumar, *Nano-Struct. Nano-Objects* **2019**, *17*, 129.
[60] N. M. Kovalchuk, D. Johnson, V. Sobolev, N. Hilal, V. Starov, *Adv. Colloid Interface Sci.* **2019**, *272*, 102020.
[61] M. Miler, B. Mirtič, *Geologija* **2013**, *56*, 5.
[62] M. Li, W.-Y. Chen, X. Zhang, F. Heidet, E. J. Listwan, D. L. Rink, J. T. Listwan, Location-Dependent Mechanical Property Evaluation on Additively Manufactured Materials, Argonne National Laboratory Report, ANL/NSE-21/47, August **2021**, pp. 15–19.
[63] Y. Ha, A. Kimura, *Crystals* **2019**, *9*, 145.
[64] B. Leng, S. Ukai, Y. Sugino, Q. Tang, T. Narita, S. Hayashi, F. Wan, S. Ohtsuka, T. Kaito, *ISIJ Int.* **2011**, *51*, 951.
[65] H. R. Z. Sandim, R. A. Renzetti, A. J. O. Zimmermann, A. F. de Padilha, A. Möslang, *MSF* **2012**, *715–716*, 629.
[66] J. Chen, X. Li, L. Kang, T. Wang, L. Yi, K. Sang, Y. Lu, *J. Mater. Res. Technol.* **2024**, *32*, 1845.
[67] Y. Ijiri, N. Oono, S. Ukai, S. Ohtsuka, T. Kaito, Y. Matsukawa, *Nucl. Mater. Energy* **2016**, *9*, 378.
[68] F. Li, L. Li, Q. Fang, J. Li, B. Liu, Y. Liu, *J. Mater. Sci.* **2020**, *55*, 13414.
[69] J. Ren, L. Yu, Y. Liu, C. Liu, H. Li, J. Wu, *Materials* **2018**, *11*, 3.
[70] W. L. Baun, *Science* **1963**, *140*, 1330.